Effect of Powder Recycling on Defect Formation in Electron Beam Melted Alloy 718

(article starts on next page)

Effect of Powder Recycling on Defect Formation in Electron Beam Melted Alloy 718

HANS GRUBER, COSMINA LUCHIAN, EDUARD HRYHA, and LARS NYBORG

The extent to which powder recycling can be permitted before risking a loss in performance of critical components is a major aspect for the viability of electron beam melting (EBM). In this study, the influence of powder oxidation during multi-cycle EBM processing on the formation of oxide-related defects in Alloy 718 is investigated. The amount of defects and their distribution in samples produced from virgin and re-used powder is studied by means of image analysis and oxygen measurements. Morphological analysis using scanning electron microscopy is performed to understand their origin and formation mechanism. The results indicate a clear correlation between the powder oxygen content and the amount of oxide inclusions present in the investigated samples. The inclusions consist of both molten and unmolten Al-rich oxide which originates from the surface of the recycled powder. Upon interaction with the electron beam, the oxide tends to cluster in the liquid metal and form critical sized defects. Hot isostatic pressing can be successfully used to densify samples produced from virgin powder. However, in the material fabricated from recycled powder, a considerable amount of damage relevant oxide inclusion defects remain after HIP treatment, especially in the contour region. It is suggested that the quality of EBM-processed Alloy 718 is at present dependent on the oxygen level in the powder in general, and on the surface chemistry of the power in particular, which needs to be controlled to maintain a low amount of inclusions.

I. INTRODUCTION

ELECTRON beam melting (EBM®) is a powder bed fusion (PBF) process in which a high power electron beam is used to melt metal powder layer by layer. Compared to the laser-based processes, EBM has a higher productivity and a lower amount of residual stresses in the built components. It is potentially well suited for the aerospace industry, especially for production of high-end, structurally optimized components made from expensive materials where traditional manufacturing is inefficient and challenging, as for the Ni-Fe-base superalloy Alloy 718.[1–4]

Currently, Alloy 718 (also known as INCONEL® 718 or IN718) is the predominant superalloy in the world. It is extensively used in the hot sections in aerospace engines as well as in the automotive, oil and gas industries. Alloy 718 stands out for its high strength, corrosion resistance, a wide operating temperature spectrum (from cryogenic up to around 650 °C), and

notably good welding characteristics.[5,6] However, such high-performance materials often suffer from difficulties during fabrication. Castings, for example, typically exhibit coarse, segregated, and porous microstructures which require homogenization and densification to reach the requirements for critical components.[7,8] In addition, its high strength and ductility make subsequent forging and machining operations inconvenient.[9,10] Furthermore, an intrinsic problem in heavily alloyed superalloys is the tendency to form non-metallic inclusions, which may cluster into larger sized defects during liquid metal processing.[11] Such clustered non-metallic inclusions are known to have a strong effect on the fatigue life of rotating parts.[1,12,13] As very little modification of non-metallic inclusions is possible through subsequent heat treatments, the number, size, and distribution of non-metallic inclusions need to be controlled in the melting process.

Additive manufacturing is characterized by a small-sized, rapidly solidified feedstock material,[13] high solidification rates (usually in the range of 10^4-10^6 K/s for laser and electron beam powder bed fusion,[14] compared to 10^0-10^2 K/s for any bulky casting process[2]), as well as a comparably small amount of material in liquid state at any one time.[2] These are all attributes that limit the size of non-metallic inclusion defects that may form during the process. It is in this

HANS GRUBER, COSMINA LUCHIAN, EDUARD HRYHA and LARS NYBORG are with the Department of Industrial and Materials Science, Chalmers University of Technology, Rnnv. 2A, 412 96 Gothenburg, Sweden. Contact e-mail: hans.gruber@chalmers.se

sense a potential candidate for production of high-performance components. However, it has been reported that oxide inclusions may occur in components fabricated by both laser[15–17] and electron beam[18] additive manufacturing. Their presence may inhibit proper wetting in-between successive layers and act as fatigue crack nucleation sites.[18]

Furthermore, the cost-effectiveness of AM relies on recycling of the non-consumed, excess powder that has been located inside the process chamber. For laser-based Alloy 718 AM processes, it has been noted that powder recycling may lower the sample ductility due to oxygen up-take during powder re-use.[19,20] However, studies dedicated to the mechanisms behind formation of non-metallic defects in EBM-fabricated Alloy 718, especially in connection to powder recycling, are very scarce. Despite this, it has been stated that the EBM excess powder can be re-used many times without any critical influence on its chemical and physical properties.[21,22] However, as shown in later studies,[23] an increased amount of oxide on the surface of the Alloy 718 powder as a consequence of powder recycling is shown to increase the amount of oxide inclusions in EBM-fabricated solid samples. As most details regarding this matter remain unclear, the aim of this study is to find the correlation between multi-cycle powder re-use and the amount and distribution of oxide-related defects in EBM-processed Alloy 718, as well as to determine its formation mechanism.

II. MATERIALS AND METHODS

The powder used for EBM sample production was a commercial, pre-alloyed, and plasma atomized powder provided by Arcam AB, Sweden, with a powder size distribution in the range of 45-105 μm. Its nominal chemical composition, presented in Table I, conforms to Alloy 718 according to standard specifications such as AMS 5662 and AMS 5596.

Solid samples were built using an ARCAM A2X EBM system, with a 4.2 melting theme version, located at University West, Trollhättan, Sweden. First, the approximately 1-mm-wide contour region was created by applying three high-energy spot melting passes (called multi-spot) around the sample edges. This was followed by a bi-directional scanning exposure at the sample core, referred to as the hatch exposure. The scan direction in the hatch region was rotated by approximately 72 degrees between each layer. Overlapping between the hatch and contour regions is done to improve the density at the interface. The EBM process operates at a partial vacuum level of around 10^{-6} bar, at a powder bed temperature of 975 ± 25 °C.[6] After operation, due to the high temperature, the fabricated parts are surrounded by an agglomerate of non-consumed powder in the form of a sintered cake that must be "recovered" before it can be re-used in the subsequent cycle. The recovery process involves grit blasting to separate individual powder particles that are sintered together in the powder cake, mixing with the non-consumed powder from the powder hoppers and finally sieving to remove any powder agglomerates with sizes above 150 μm. For each build cycle, before filling the powder into the powder hoppers, a small powder sample (below 10 g) was collected for microscopy and chemical analysis. A more detailed description of the EBM and the powder recovery processes can be found in References 6 and 22.

The solid samples studied in this work were produced in four sequential build cycles. The powder feedstock was characterized for its oxygen content before starting the build, which increases steadily with powder re-use, see Table II. The build cycles in which the samples were produced, as well as the total (accumulated) process time of all preceding cycles, serve as additional information, but are only rough indicators of the powder condition. The first cycle was started with 80 kg of virgin powder from which the first sample set, B1, was produced. The two following sets, B6 and B14, were also produced from this powder batch, with powder recovery in-between the cycles. 20 pct virgin powder was added before cycle 6. After this, no virgin powder was added. The B30 samples were produced from a mixture of heavily recycled powder which had been exposed to up to 30 times of powder recycling, which corresponds to a total process time of around 1000 hours.

Table I. Chemical Composition of the Alloy 718 Powder as Provided by the Powder Producer

Element	Ni	Co	Cr	Mo	Ti	Mn	Nb	B	P	Ta	Al	Fe	Si	S	C
Wt Pct	54.1	0.04	19.0	2.99	1.02	0.12	4.97	0.001	0.004	< 0.01	0.52	17.12	0.06	< 0.001	0.03
At. Pct	53.38	0.04	21.16	1.80	1.23	0.13	3.10	0.01	0.01	< 0.01	1.12	17.75	0.12	< 0.001	0.14

Table II. Build Cycle Information with Powder Oxygen Levels, Obtained from Combustion Analysis

Sample Designation	Average Powder Oxygen Level, ppm	Individual Powder Oxygen Measurements, ppm	Build Cycle No.	Accumulated Process Time, Hours
B1	146	131, 148, 159	1	0
B6	195	185, 196, 204	6	220
B14	266	257, 264, 277	14	500
B30	312	282, 297, 357	30	≥1000

Hot Isostatic Pressing (HIP) of the EBM-fabricated samples was performed at a temperature of 1200 °C, applying a pressure of 1000 bar for 4 hours. The HIP was performed on courtesy of Quintus Technologies AB, Västerås, Sweden.

Characterization of the virgin and re-used powder samples was performed with focus on the change in powder surface chemistry and morphology during powder recycling. This was done by means of scanning electron microscopy (SEM), using a Leo Gemini high-resolution SEM (LEO GmbH, Oberkochen, Germany) equipped with a secondary electron in-lens detector. A solid-state-dispersive X-ray spectrometer (EDS) from Oxford Instruments (X-Max, Oxford Instruments Ltd, High Wycombe, UK) was used for qualitative micro-chemical analysis. Surface characterization was performed on samples that were prepared by slightly pressing powder particles into aluminum plates. Non-metallic inclusions inside the powder were analyzed by light optical microscopy (LOM) and SEM/EDS on powder cross-sections. Powder cross-sections were prepared from a mixture of powder and conductive bakelite resin that was mounted, grinded, and polished according to standard metallography recipes.

The solid samples had a geometry of $11 \times 11 \times 60$ mm^3 and were built with the longitudinal direction parallel to the build direction using standard scan strategies and process parameters. From these samples, standard Charpy V-notch (CVN) test bars with a geometry according to ASTM standard E2316-b were machined. The samples were fractured using an Instron Wolpert PW30 impact tester with a capacity of 300 J located in Höganäs AB, Höganäs, Sweden. Fractography, by means of SEM/EDS, was performed in as-printed condition to study the morphology of defects in samples produced from powder material with varying oxygen content.

For each set of solid samples, metallographic cross-sections from three individual samples were evaluated in terms of defect density and distribution of defects parallel and transversal to the build direction, in both as-printed condition and after HIP. As compared to as-printed samples, quantification of non-metallic inclusions in the as-HIP samples can be done by image analysis since porosity and lack of fusion defects (LOFDs) enclosed in the material are removed during the HIP cycle. As voids connected to the outer surface will not be consolidated, the contour region in the as-HIP samples was carefully studied so that open porosity could be distinguished from oxide inclusions, which appear shiny gray in the LOM. In this way, areas which contained surface connected voids could be disregarded from the measurements. The defect density was measured on cross-sections positioned according to Figure 1(a), i.e., transversal to the building direction at a distance around 5 mm from the top and bottom surface, respectively. For each cross-section, a set of at least 12 randomly distributed images were captured in each of two different regions, as indicated in Figure 1(b): the interior (or core) part of the sample (the hatch region) and in the area up to around 1.5 mm from the outer surface, i.e., in the region inside or close to the contour region (for convenience hereafter called contour region). The images were captured at $\times 100$ magnification using a Leica DMRX light optical microscope. In total, an area of at least 50 pct of the total cross-section area was covered. Image analysis was performed using the software ImageJ by applying a threshold to produce binary images allowing for defect quantification. For each region (hatch and contour), the total defect area of all analyzed images was summed up and presented as the fraction of the total analyzed area.

Detailed morphological characterization and micro-chemical analysis of selected cross-sections was performed by SEM and EDS. As part of the characterization of the defect distribution, the sample top surface was studied in terms of amount of non-metallic phases together with their location relative to the solidification structure of the last solidified layer. The latter was performed on cross-sections parallel to the build direction that was cut perpendicular to the scan tracks in the last solidified layer. The solidification structure was
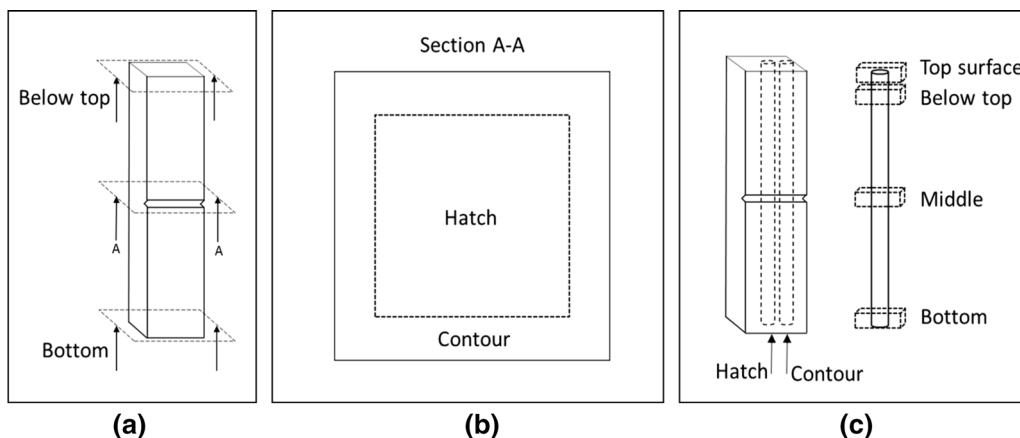

Fig. 1—Positions within the solid EBM samples evaluated in terms of (a) and (b) metallographic image analysis and (c) oxygen and nitrogen measurements. Cross-section A-A in (a) presented in (b).

revealed by electrolytic etching with oxalic acid for around 10 s at a voltage of 3 Volts. All cross-sections were prepared according to standard metallographic procedures.

Oxygen and nitrogen measurements of powder and solid samples were performed by means of inert gas fusion (combustion analysis) on a LECO ON836 elemental analyzer, to quantify the extent of oxidation of progressively re-used powder as well as amount and distribution of non-metallic inclusions in the solid samples. In the latter, for each set of samples, the bulk concentrations were measured in 5 mm long Ø 4 mm cylinders that were machined out from the sample center part. Furthermore, the distribution of oxide and nitride inclusions along the build direction within some selected solid samples was evaluated by comparing the O and N levels at four positions along the sample center line, as shown in Figure 1(c). For the same reason, the O, N concentrations in samples extracted from the hatch and the contour regions were compared. Oxygen and nitrogen measurements were performed in accordance with the standards SS-EN 10276-2 and SS-EN ISO 15351, respectively. For each sample set, at least three individual samples were evaluated.

III. RESULTS

A. *Powder Characterization*

Scanning electron micrographs of the virgin-state Alloy 718 powder are shown in Figure 2. As seen in Figure 2(a), this powder generally has a clean surface appearance that is visually free from non-metallic phases. Even though being fairly few in number, non-metallic inclusions with an equivalent diameter of around 1-10 μm can be observed in the powder when studied at higher magnifications. Powder cross-section analysis shows that they often consist of a dual-phase structure comprising a nucleus and an outer rim, see Figure 2(c).

A close coincidence between the outer rim and the Ti and N images in the EDS map in Figure 2(d) identifies it as TiN. Similarly, a high amount of Al and O in the
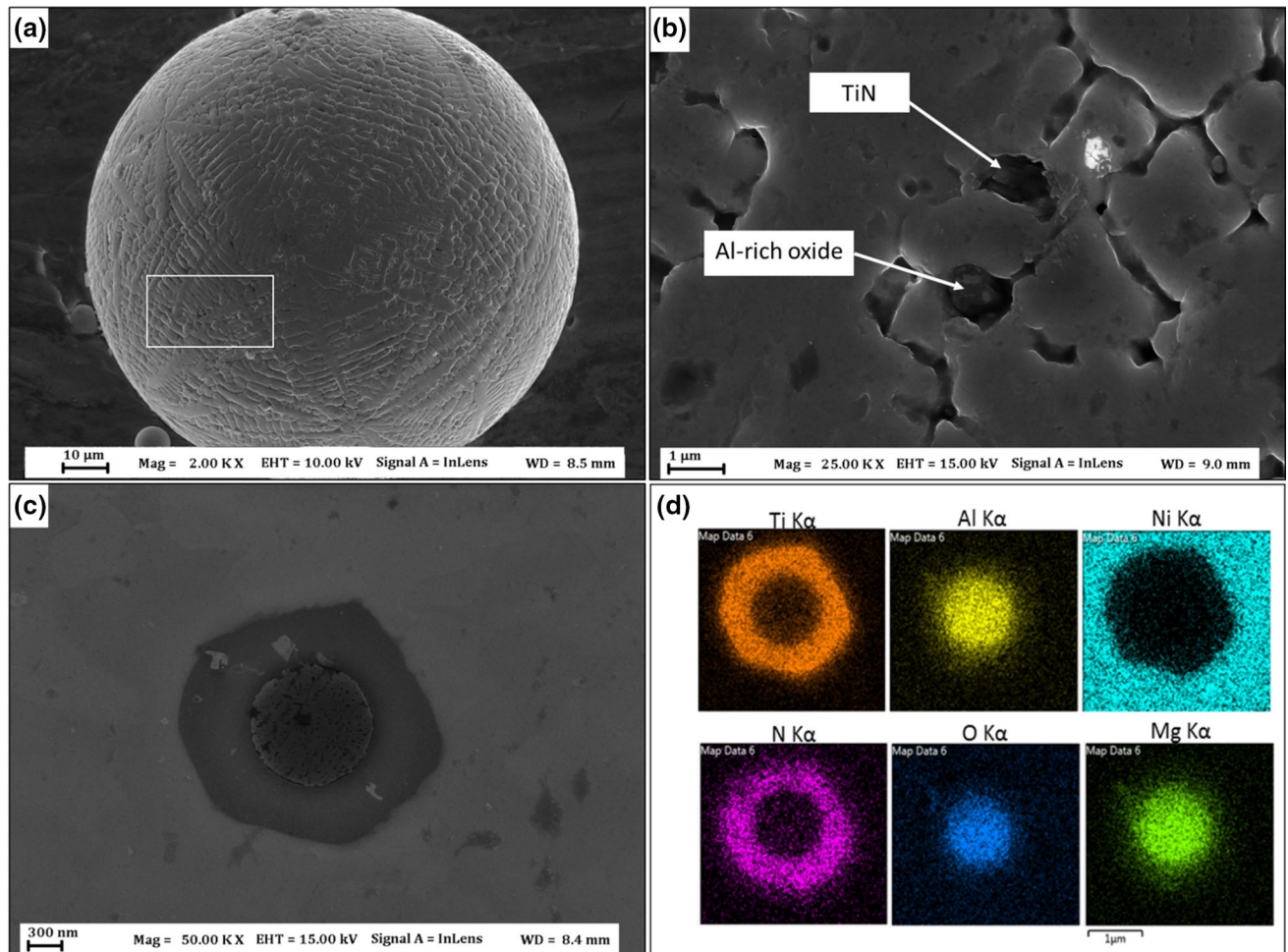

Fig. 2—Scanning electron images of the virgin powder; (*a*) secondary electron micrograph of the powder surface; (*b*) surface at higher magnification showing non-metallic inclusions; (*c*) secondary electron micrograph of a composite TiN/Al-rich oxide inclusion on a powder cross-section; (*d*) EDS map of the inclusion in (c).
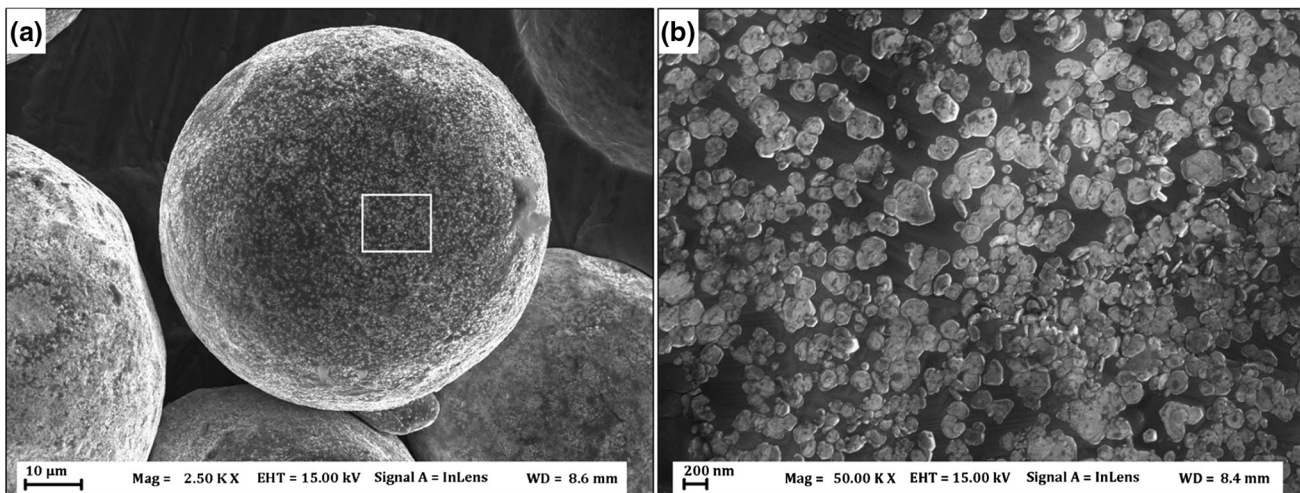
Fig. 3—(a) Secondary scanning electron image of the powder before build cycle 30; (b) Al-rich oxide particulates on the surface at higher magnification.
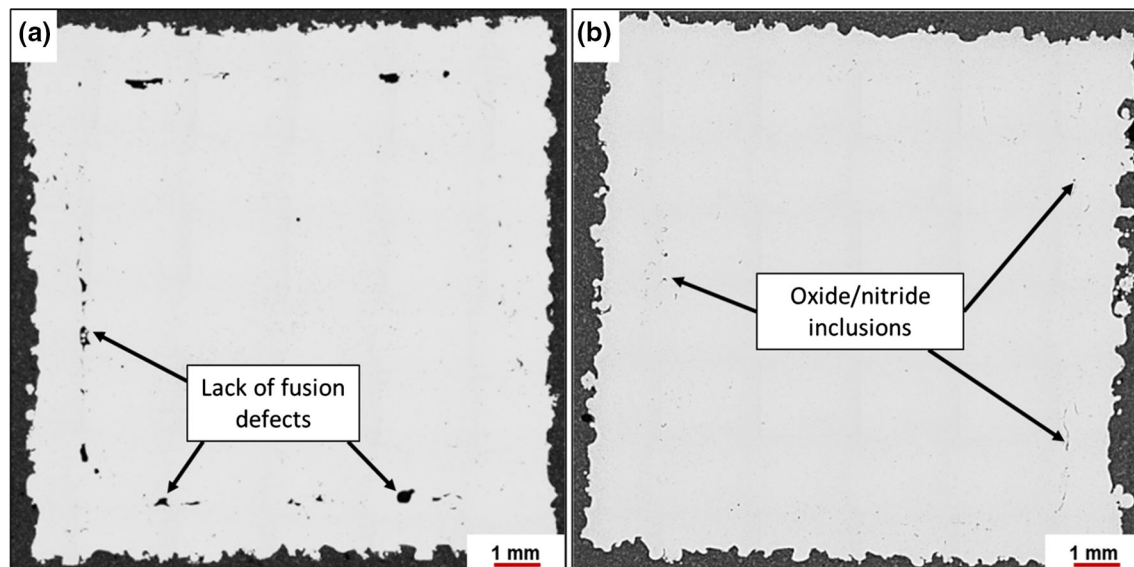

Fig. 4—Light optical micrographs of B30 CVN specimens showing typical distribution of defects on cross-section transversal to the build direction; (a) as-printed condition; (b) as-HIP condition.

nucleus identifies it as Al-rich oxide. The strong oxide forming element Mg, which is a trace element in the studied material (see Table I), was also occasionally detected in the oxide nuclei, see Figure 2(d). Single phase oxide and nitride particles were observed as well. Similar non-metallic inclusions were observed on the cross-sections of the recycled powder.

Figure 3 shows the surface of a powder sample collected before build cycle number 30. As was already described in previous research,[23,24] a significant part of the re-used Alloy 718 powder surface is covered by Al-rich oxide particulate features that have formed during exposure of the powder to the process and the environment in the EBM build chamber. In Reference 24, it was also shown that the oxide particulates are confined to the powder surface. A more detailed characterization of the virgin and recycled Alloy 718 powder surface can be found in Reference 24.

B. Characterization of Defects in the EBM-Fabricated Material

Cross-section transversal to the build direction of a B30 specimen in as-printed condition as well as after HIP treatment is shown in Figures 4(a) and (b), respectively. In both cases, larger sized lack of fusion defects and non-metallic inclusions are mainly found along the interface between the contour and hatching regions at around 1 mm from the outer surface. This defect distribution is representative for samples produced from both virgin and re-used powder.
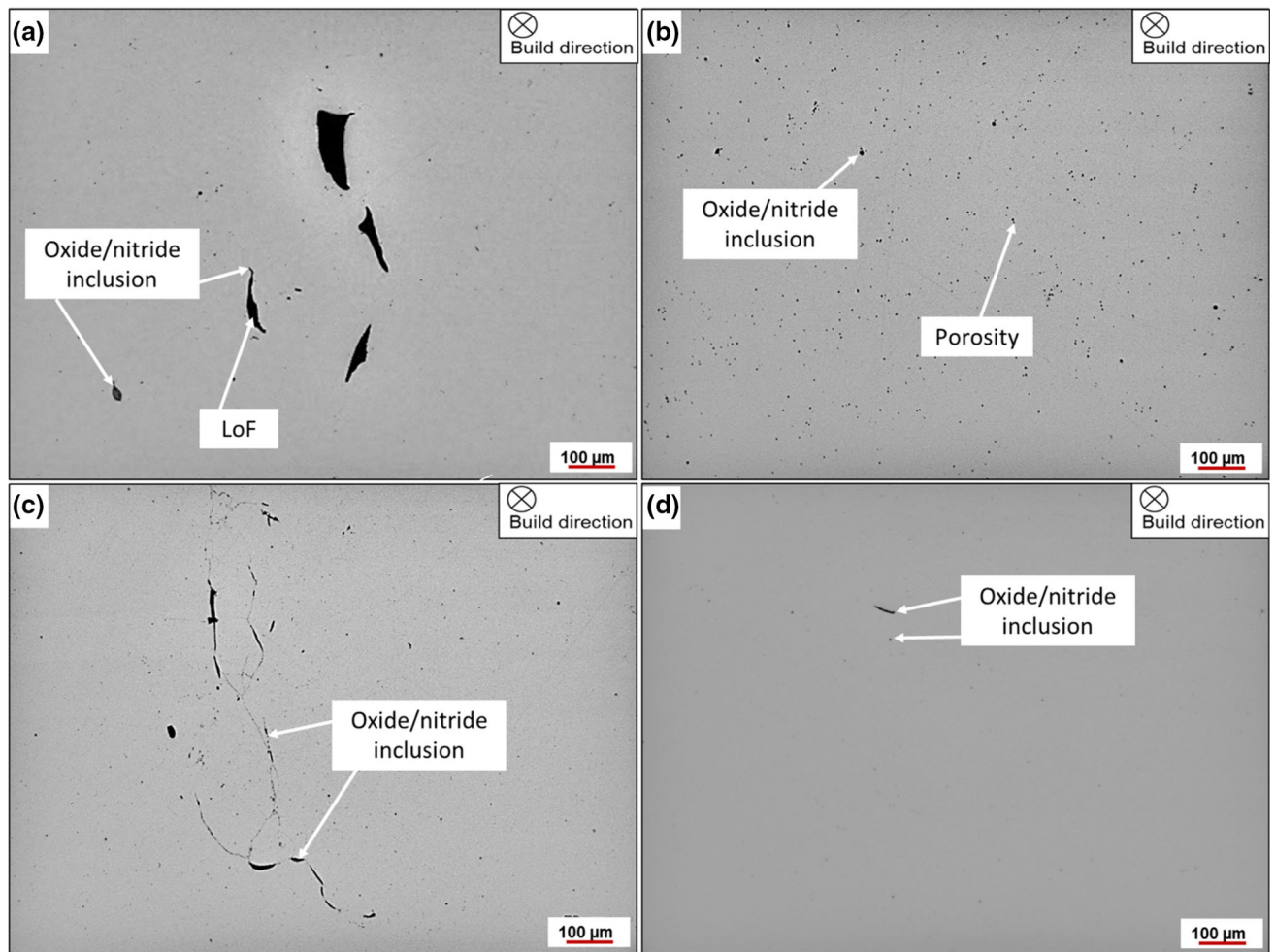
Fig. 5—Light optical micrographs showing defects in the B30 samples; (*a*) as-printed, contour region, (*b*) as-printed, hatch region (*c*) as-HIP, contour region, (*d*) as-HIP, hatch region.

In as-printed condition, the contour region often contains lack of fusion defects (LOFDs) with in-plane dimensions up to several hundred micrometers. Oxide/nitride inclusions often appear inside LOFDs, as shown in Figure 5(a). TiN inclusions are easily observed due to their yellow tinge and blocky shape in the LOM. Similarly, the oxide has a gray, shiny appearance which makes it distinguishable from porosity and LOFDs. The hatch region mainly contains large amounts of pores, see Figure 5(b). As shown in Figures 5(c) and (d), the defect density after HIP is significantly lower due to elimination of enclosed LOFDs and porosity. Except for voids connected to the outer surface, only non-metallic inclusions remain in the samples after HIP. Also in this case, the largest inclusions, with in-plane dimensions up to several hundred micrometers, are found close to the contour region, Figure 5(c). As seen in the electron images in Figure 6, as a consequence of LOFD consolidation, a network of non-metallic inclusions is left behind, both in the form of individual oxide particulates and as agglomerated oxide and nitride phases. Defects in the hatch region usually consist of discrete TiN and clusters/agglomerates of oxide and Ti-rich nitride inclusions, see Figure 7. As will be shown below, the amount

of non-metallic inclusions increases with progressive powder re-use.

Typical morphologies of non-metallic agglomerated defects in the hatch region are shown in Figure 7. In the plane transversal to the build direction, they have a random orientation and shape, see Figure 7(a). When studied on cross-sections parallel to the build direction, they often have an elongated shape, with the major axis orientated perpendicular to the build direction, see Figure 7(c). In this direction, they can reach a few hundred micrometers. Larger sized inclusions are found in samples produced from re-used powder. Their thickness is usually in the range of a few microns, see Figures 7(c) and (d). As seen in the EDS map in Figure 7(b), the inclusions mainly consist of agglomerated Al-rich oxide, decorated with titanium nitride particles at the rim between the matrix and the defect. The EDS point analysis in the oxide-rich areas, such as point B in Figure 7(d), often gives a chemical composition close to that of pure alumina, see Table III. These findings have been confirmed from chemical analysis of a large number of inclusions in many different samples.

In agreement with previous observations,[23] fractography in the plane transversal to the build direction
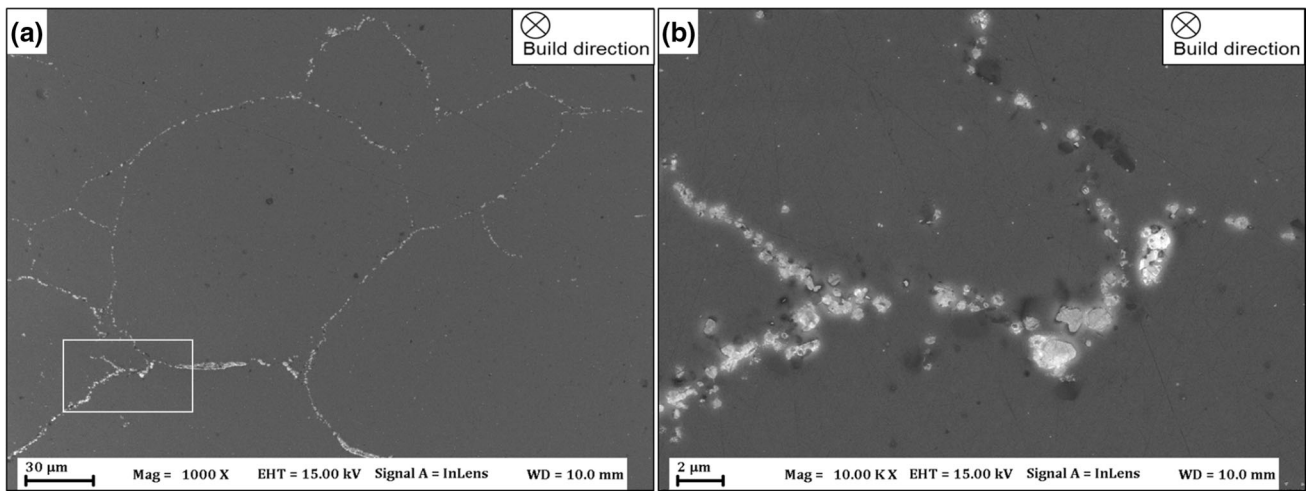
Fig. 6—(a) and (b) Secondary scanning electron images of a B30 sample in as-HIP condition showing non-metallic inclusions in a densified LOFD on a cross-section transversal to the build direction; higher magnification in (b).
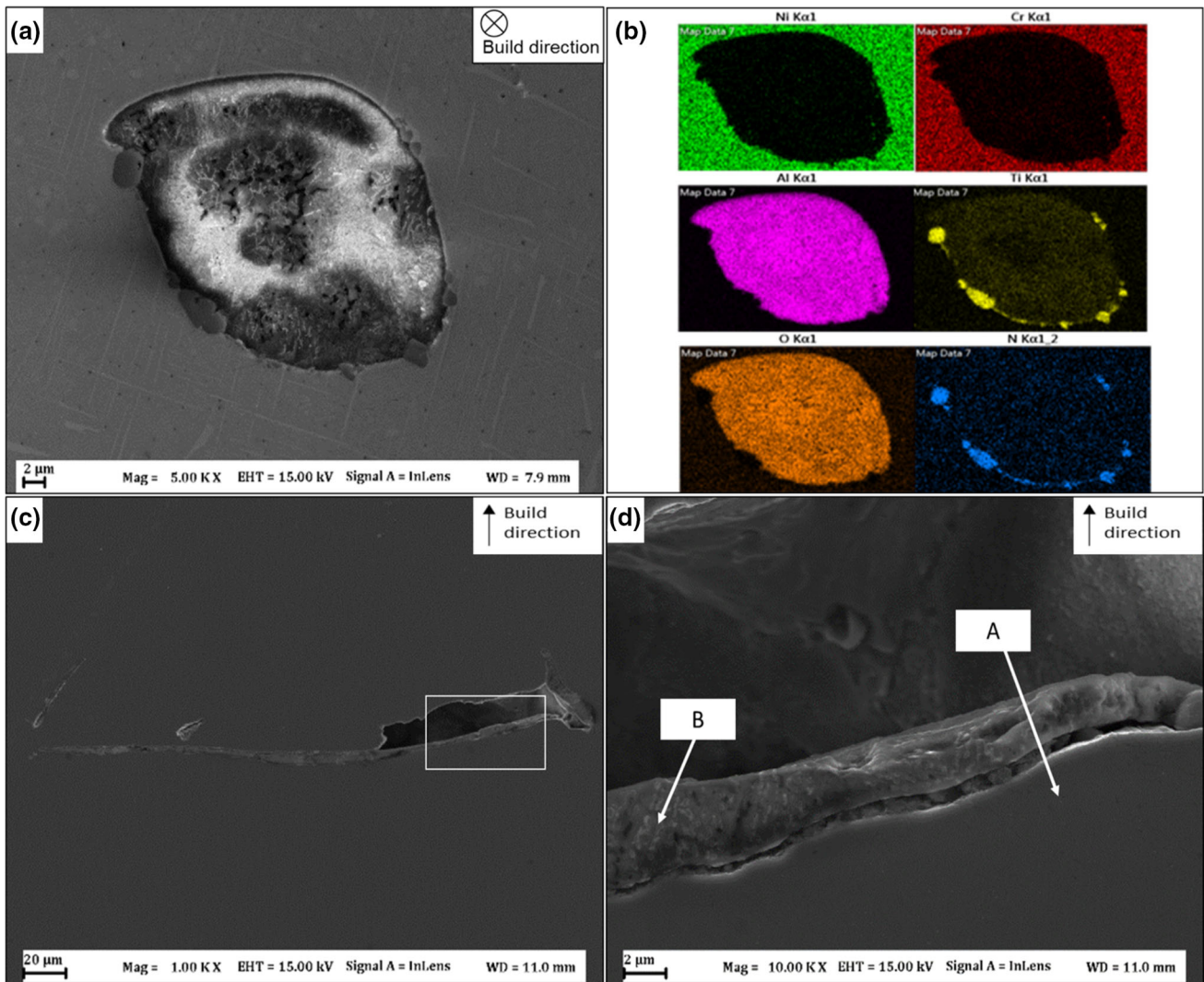

Fig. 7—Non-metallic inclusions observed in the hatch region of samples in as-printed condition; (a) oxide/nitride defect on a cross-section transversal to the build direction in a sample built from virgin powder; (b) corresponding EDS map; (c) large, planar oxide inclusion on a cross-section parallel to the direction in a B30 sample; (d) inclusion in (c) at higher magnification with EDS point analysis regions.
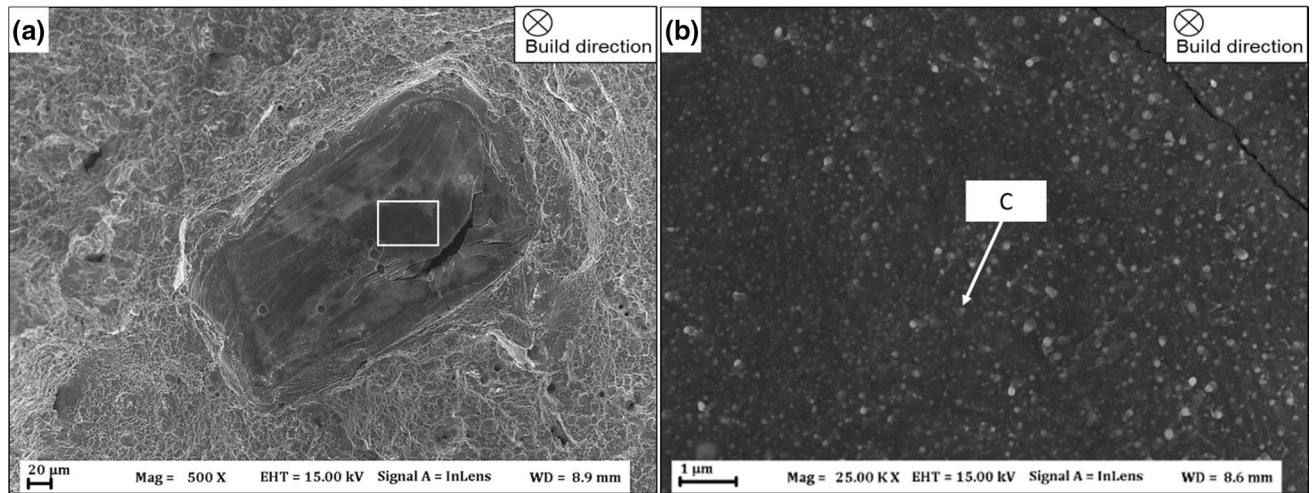
Fig. 8—(a) Non-metallic inclusion in the hatch region of a fractured B30 sample in as-printed condition; (b) higher magnification image showing its homogeneous structure. Chemical composition measured in point C is presented in Table III.

Table III. EDS Analysis Data Obtained from Matrix and Oxide Inclusions in Figs. 7 and 8

Location	Structure	Element	Chemical Composition							
			Ni	Cr	Fe	Nb	Mo	Ti	Al	O
A	gamma matrix	wt pct	51.6	18.7	19.2	5.3	3.1	1.3	0.8	—
		at. pct	50.9	20.8	19.9	3.3	1.9	1.6	1.7	—
B	Al-rich oxide inclusion	wt pct	1.9	1.2	—	—	—	6.9	47.3	42.8
		at. pct	0.7	0.5	—	—	—	3.1	37.9	57.8
C	Al-rich oxide inclusion	wt pct	8.5	4.0	3.3	1.6	—	5.5	37.9	39.2
		at. pct	3.4	1.8	1.4	0.4	—	2.7	32.9	57.4

clearly reveals that samples produced from re-used powder often contain large, planar oxide inclusions. Thus, together with the typical oxide morphology on cross-sections parallel to the build direction, see Figures 7(c) and (d), it can be concluded that most large inclusions have a flake-like shape. It is important to note that such inclusions in the material fabricated from virgin powder are considerably fewer and smaller. Figure 8 shows the fracture surface of the hatch region in a B30 sample with the presence of a large planar Al-rich oxide inclusion, which has suffered from extensive cracking. Its homogeneous appearance and the cracks that span across its whole length indicate that it consists of a continuous phase that has formed from accumulation of melted oxide. A representative chemical composition of such flake-shaped inclusions, obtained from EDS analysis, is presented in Table III.

C. Quantity and Distribution of Non-metallic Inclusions in the EBM-Fabricated Material

1. Defect Density Measurements

The defect density in solid samples produced from virgin and progressively re-used powder, in as-printed and as-HIP condition, is presented in Figure 9(a). As seen here, only as small portion of the defects present in

as-printed condition remain after HIP, which, for improved visualization, is presented separately in Figure 9(b). As seen in Figure 9(a), there is a steady increase in defect density in the contour region with respect to progressive powder re-use. This is mainly due to an increasing amount of LOFDs, which is considerably lower in samples built from virgin powder.

Also after HIP, there is a steady increase in defect density in the contour region with respect to progressive powder re-use, see in Figure 9(b). This is in line with the increased amount of inclusions in consolidated LOFDs, but also other large oxide agglomerations, as shown in Figure 5(c). A much more modest increase in defect density is seen in the hatch region, in agreement with the result presented in Figure 5(d).

The increasing amount of oxide phases in powder and solid samples as a result of powder re-use is also detected when measuring the oxygen level in progressively re-used powder and corresponding hatch regions of the solid samples, as shown in Figure 10. Clearly, there is a steady increase in oxygen in both powder and solid samples as a consequence of powder re-use. A lower oxygen level (around half) is seen in the solid sample bulk compared to their parent powder material. The nitrogen level, on the other hand, is relatively stable at around 150 ppm in both power and solid
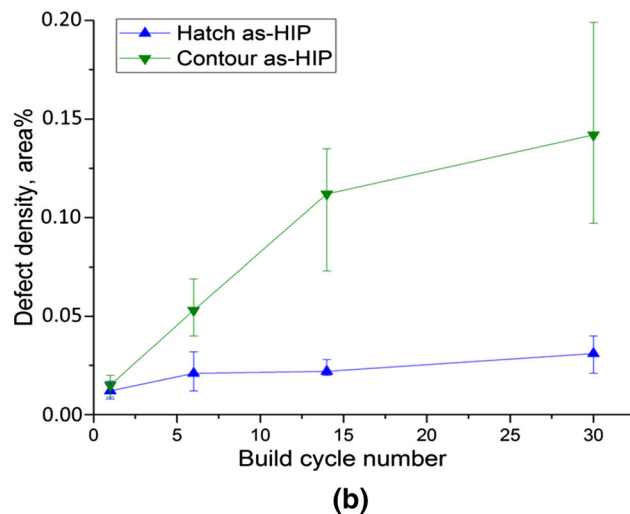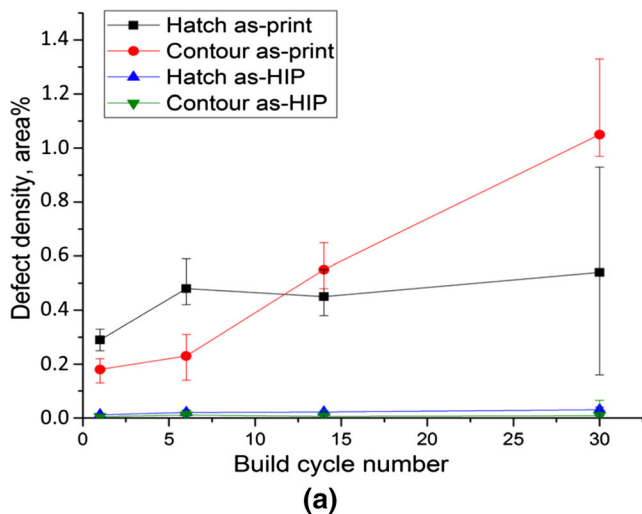
Fig. 9—Defect density in the hatch and contour region measured in (*a*) as-printed and as-HIP condition (*b*) as-HIP condition. The error bars indicate the actual measurement range. All data points are average values obtained from measurements in the cross-sections "bottom" and "below top", as indicated in Fig. 1(b).
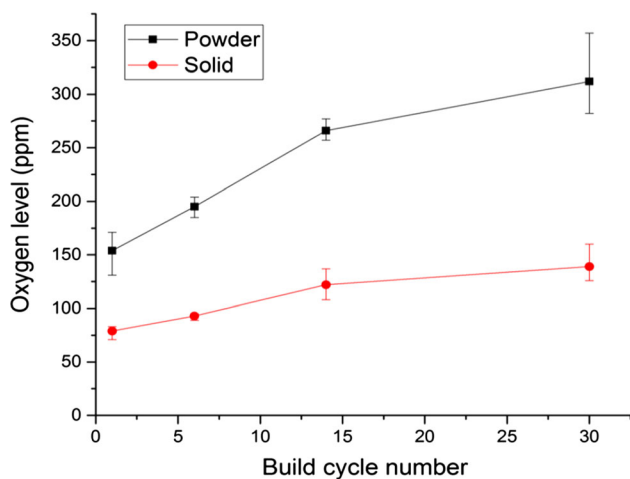

Fig. 10—Oxygen level in powder and solid samples with respect to progressive powder re-use. The oxygen level in the solid samples is measured in the middle hatch position, see Fig. 1(c). The error bars indicate the actual measurement range.

samples irrespective of the condition of the powder and is therefore not included in the graphs. This indicates that the amount of nitrogen-containing phases (mostly TiN) is stable during both powder recycling and electron beam melting.

2. Oxide Distribution

Figures 11(a) and (b) show the sample top surface (last melted layer) of a B30 sample, which contains a large amount of Al-rich oxide. EDS point analysis on the dark regions in Figure 11(b) gives a similar composition as from the oxide inclusions present in the bulk of the samples (see Table III). The oxide is arranged as strings in a regular pattern aligned along the electron beam scan direction and is often positioned close to the

center of the melt pool top surface. This is also seen when studying the cross-section of the top surface, see Figure 11(c), where the oxide strings have been indicated with arrows. In the higher magnification image in Figure 11(d), a string of oxide which smoothly follows the top of the melt pool in the last solidified layer is shown. As can be seen here, clusters of TiN particles are commonly present together with the oxide. Moreover, from Figure 11(a) it is clear that accumulation of oxide especially takes place at the end of the hatch lines. This observation further explains the large amount of oxide impurities at the interface between the hatch and contour region, as was shown in Figure 9. As compared to the clean appearance of the B1 sample top surface, shown in Figures 11(e) and (f), it is clear that the top surface of samples produced from re-used powder contain much more oxide than their virgin powder counterparts. As the amount of oxide in Figure 11(a) and (b) is much larger than what is observed inside the bulk material, see for example Figure 5(d), it is reasonable to expect that oxide is transported upwards towards the top surface during the melting process.

The extent to which non-metallic inclusions accumulate in certain positions within the material was measured in terms of metallographic image analysis as well as oxygen analysis, see Figure 1(a). The results for a set of three B30 samples are shown in Figure 12. As already indicated in Figure 5, image analysis shows that the defect density in the contour region is continuously higher than in the hatch, see Figure 12(a). In the same figure, it is also shown that image analysis could not detect a clear difference in defect density between the bottom and top part, neither in the contour nor in the hatch region. The oxygen measurements presented in Figure 12(b), on the other hand, suggest a slight increase in oxygen level along the build direction of the hatch material. Especially, the top surface clearly shows
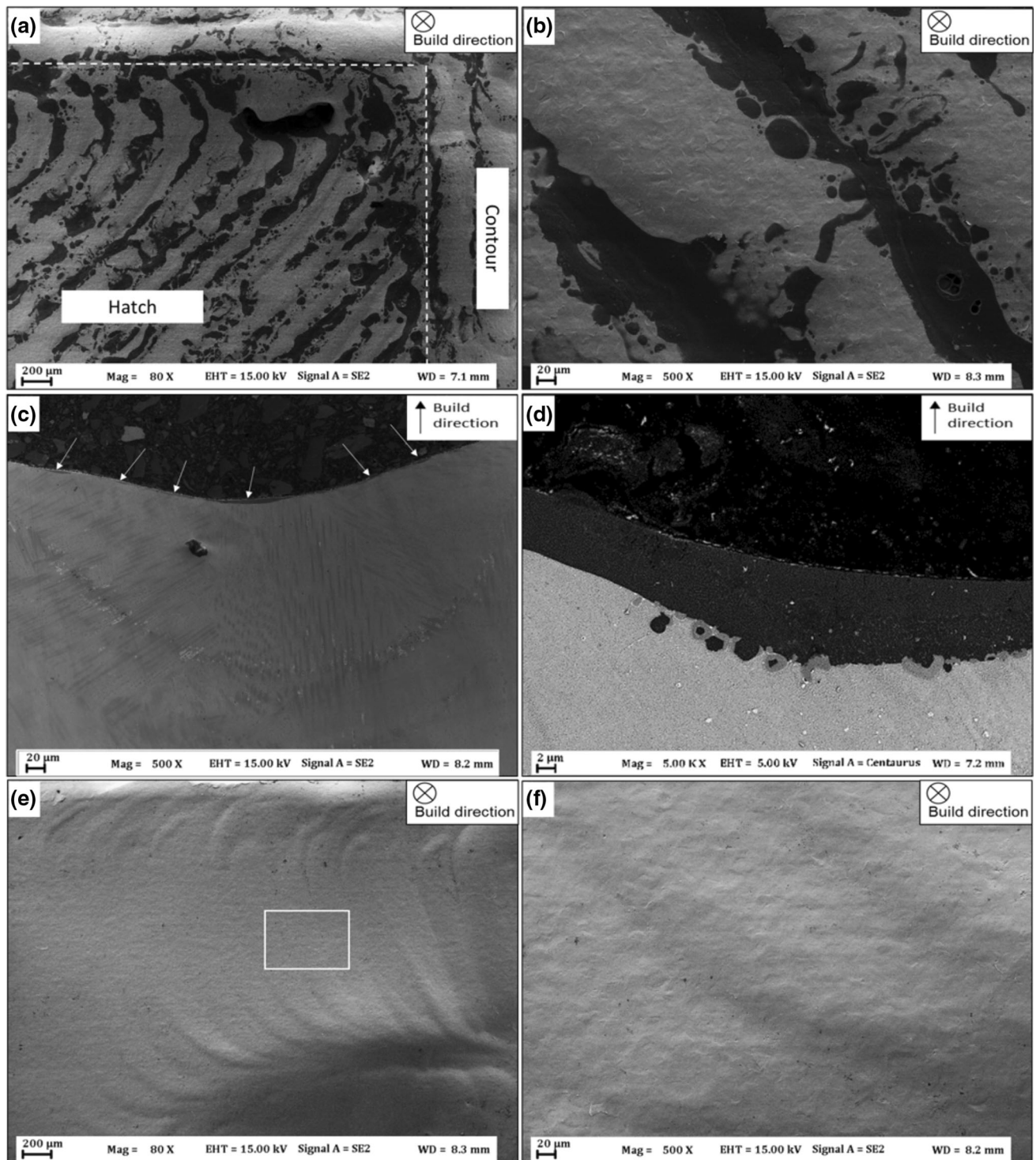
Fig. 11—Scanning electron micrographs showing the top layer of the EBM-fabricated samples; (*a*) top view of a B30 sample; (*b*) top view of oxide strings at higher magnification; (*c*) top layer of a B30 sample observed on a cross-section parallel to the build direction with oxide strings indicated with arrows; (*d*) cross-section of an oxide string at higher magnification; (*e*) and (*f*) top view of a B1 sample.

consistently higher oxygen levels, in agreement with the observed accumulation of oxide on the top surface, as shown in Figure 11. Also in this case, the continuously higher oxygen level in the contour (middle contour) as compared to the hatch (middle hatch) confirms the accumulation of non-metallic phases in the contour region as shown in Figure 12(a).

IV. DISCUSSION

The effect of powder recycling on the amount of defects in EBM-processed Alloy 718 has been presented above. The results indicate a clear correlation between defect density, both oxide inclusions and LOFDs, and the powder oxygen level, which increases with
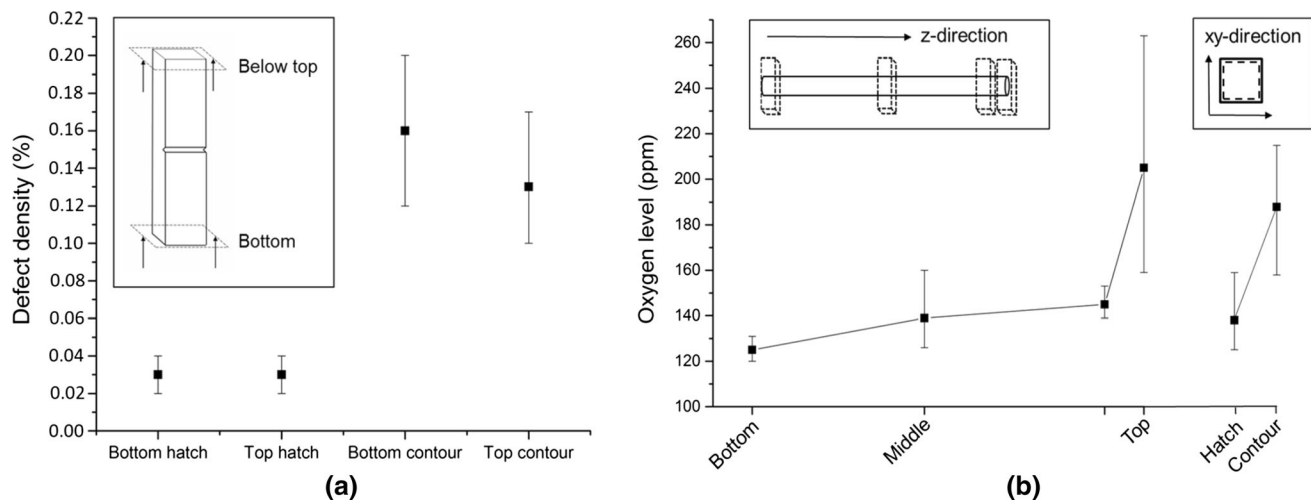
Fig. 12—(*a*) Defect density and (*b*) oxygen measurements along the build direction and in the hatch and contour regions in as-HIP B30 samples. The oxygen level in the middle hatch in (b) is the same as the value presented in Fig. 10. The error bars indicate the actual measurement range.

progressive re-use. The significantly larger amount of oxide inclusions in the specimens fabricated from re-used powder suggests that the feedstock powder is the main oxygen source for oxide formation during the EBM process. This stands in contrast to studies on other additive manufacturing processes (such as laser powder bed fusion (LPBF) and direct energy deposition (DED)), where free oxygen in the process atmosphere is often reported to be the critical factor for oxide formation.[15,17] In Thijs *et al.*,[17] for example, the formation of Al- and Ti-rich oxide inclusions during LPBF processing of a maraging steel was explained to occur due to oxygen from the process atmosphere, which dissolves in the melt where it reacts with Ti and Al in the steel. According to Ding *et al.*,[15] similar events take place during wire arc DED of a similar material.

Regarding electron beam processing of Alloy 718 in both wire and powder condition, the presence of agglomerated oxide and nitride defects has been reported in the deposited material.[2,18] In this context, it should also be noted that agglomeration of non-metallic inclusions present in liquid metal is a well-known phenomenon in the casting industry.[25] In Polonsky *et al.*,[1] the presence of agglomerated non-metallic inclusions in EBM-processed Alloy 718 was described to be a consequence of oxide and nitride inclusions present in the powder, which dissolves in the melt due to the high temperature under the electron beam (up to 3000 °C), followed by reformation and clustering upon cooling, when the solubility product is exceeded. Similar conclusions were drawn in Reference 18.

However, the situation seems to be different for the present EBM material fabricated from heavily re-used powder. As summarized in Figure 13, the oxide defects in the as-printed B30 samples can be divided into three main morphologies: dispersed inclusions, inclusion clusters, and flake-shaped inclusions. Dispersed inclusions are especially found together with oxidized, un-melted metal particles in areas where the feedstock material has not been fully melted, *i.e.*, in LOFDs. Due to the lack of

a continuous melt pool when melting the re-used metal powder under such conditions, the oxide particulates on its surface are not given the opportunity to agglomerate. Instead, as shown in Figures 13(a) and (b), they are finely dispersed on the interior surfaces of the LOFD in a configuration similar to that as seen on the powder surface, see Figure 3.

The presence of clusters of such small oxide inclusions, shown in Figure 13(c), can be justified by a higher energy input compared to the previous case. In this case, the energy input has been high enough to fully melt the metal, and hence, the particulates from the powder surface have been able to agglomerate to form clusters.

Frequent appearance of oxide clusters that are partially melted together, as shown in Figure 13(d), indicates that the energy input is locally high enough for initial melting of the oxide inclusions. Partially melted oxide inclusions are often seen in the vicinity of large, homogeneous oxide flakes, as shown in Figure 8. Even though very high temperatures may be reached, these large amounts of accumulated oxide are most likely not dissolved in the liquid metal since the solubility of oxygen is very limited.[11] Instead, when the energy density is high enough, the oxide melts and subsequently solidifies into the flake-shaped morphology as commonly observed in the samples produced from re-used powder.

Similar for all defect morphologies is the presence of oxide inclusions with the same size and shape as on the re-used metal powder. It should also be noted that EDS analysis of all studied inclusions shows chemical compositions similar to those of point B and C in Table III. Based on these observations, it is suggested that the major part of the oxide-related defects in the present material are connected to the Al-rich oxide particulates from the surface of the re-used power. The formation mechanisms are described in more detail below.

The upwards transportation of oxide and nitride through the layers towards the top surface, as shown in Figures 11 and 12, has been reported for both laser and
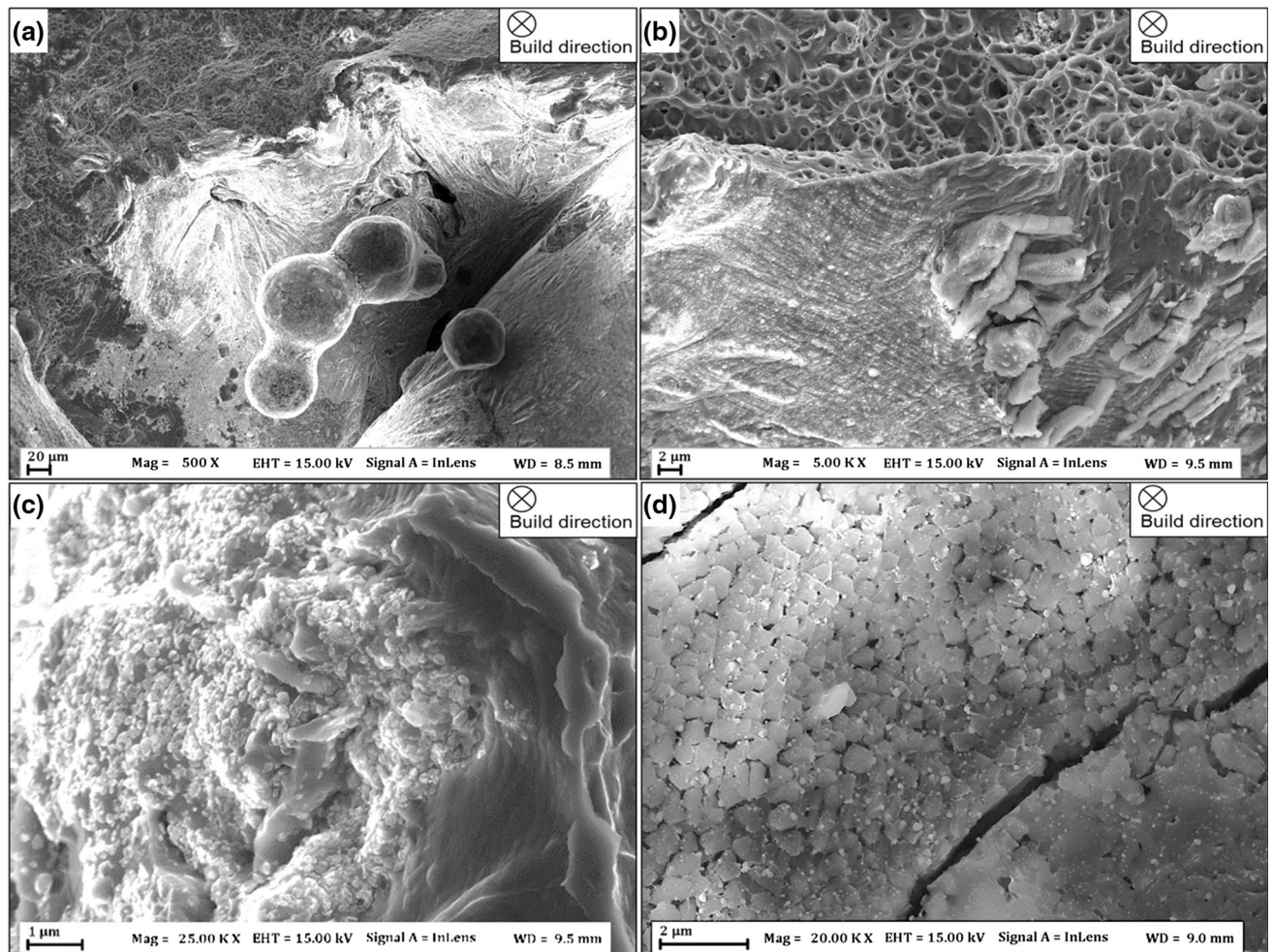
Fig. 13—(a) and (b) Interior of a LOFD as observed from a fracture surface of a B30 sample; higher magnification in (b); (c) cluster of nano-sized oxide inclusions; (d) partially melted oxide inclusions.

electron beam powder bed fusion. In the study by Thijs *et al.*,[17] this is justified mainly in terms of the buoyance effect, *i.e.*, that the oxide floats to the surface of the melt pool since its density is lower than that of the metal (~ 4.0 and ~ 5.4 g/cm^3 for Al$_2$O$_3$ and TiN, respectively,[26] compared to ~ 8.2 g/cm^3 for Alloy 718[27]). Polonsky *et al.*,[1] suggested that the high solidification rate in EBM limits the buoyance effects. Instead, the upwards transportation and clustering behavior of nitride and oxide inclusions within the melt pool is in this case explained to be dominated by thermocapillary (Marangoni) flow driven by large thermal gradients and consequently large surface tension gradients across the melt pool surface.[1,28] When the levels of surface active elements such as O and/or S exceed around 10 ppm (as in the case of the current material), the flow is directed radially inwards and towards the hotter region at the top center of the melt pool. This would explain the clustering behavior of oxide and nitride as seen in Figures 11(c) and (d).[29] A certain degree of randomness in the distribution on the top of the melt pool, as seen in Figure 11(a), is likely to occur, however, owing to the turbulence created by the flow in different

directions[30] and the extremely fast solidification times involved in EBM. Nevertheless, during melting of the subsequent layers, the oxide may be transported upwards layer by layer and at the same time agglomerate with more oxide. Finally, it may reach the top surface as shown in Figure 11.

Still, depending on the liquid flow and the size of the oxide, especially large oxide flakes may be entrapped inside the solidifying metal, which is the reason for the inclusions inside the bulk material. Cracking of large oxides into smaller pieces, as shown in Figures 8(a) and 13(b), may promote upwards transportation along the building direction.[15] Furthermore, owing to the high melting point and low thermal conductivity of the oxide phase, melting of thick oxide layers (as can be seen in Figure 7) requires much higher temperature (> 2000 °C in case of Al$_2$O$_3$) and higher energy input compared to melting the metal alloy beneath it. Therefore, when the oxide layer/flake reaches a critical size, it may not be melted and will therefore remain in its initial position, as observed in Figures 7 and 8. In such case, re-melting of the previous layers will not take place,[15,17] which will inevitably result in the formation of a LOFD. Thick

oxide layers are especially seen at the interface between the hatch and contour region, see Figure 11. This indicates that oxide is pushed along the solidification front and accumulates at the end of the scan tracks, where the electron beam changes direction. Consequently, the amount of LOFDs in the contour region increases with progressive powder re-use (Figure 9). Furthermore, since upwards transportation of oxide relies on layer re-melting, this also explains the small difference in defect density between the bottom and top parts of the contour region (Figure 12). The larger amount of oxide on the surface of the re-used powder may also lead to a reduced energy absorption and/or increased electrical resistivity between the powder particles. This may have a negative effect on the sintering behavior which may lead to an increased risk of ''powder smoking'' (ejection of powder from the powder bed), with the formation of LOFDs in the subsequent layer as a result.[1,31]

As shown in Figure 10, the oxygen level in the powder is consistently higher than that in the bulk material of the solid samples, which means that there is a net release of oxide from the bulk material during the EBM build process. The reason for this may be twofold. Firstly, as shown above, the fact that layer re-melting has a certain ability of dragging oxide towards the top surface, lowers the amount of oxide in the rest of the bulk material. Secondly, as suggested in previous research,[1,2] some degree of vacuum refining of both nitride and oxide is possible in the liquid metal at the low pressure conditions in the vacuum chamber. However, even though the temperature and the pressure are, at least theoretically, at levels where O and N may be removed from the metal,[11,13] the short duration at which the material is in liquid state limits the removal of N and O.[13,32] In addition, dissociation of the less stable oxide/hydroxide present on the powder surface (as shown in Reference 24) is likely to occur already during the powder pre-heating step. However, as described in Reference 24, it should be noted that the released oxygen may as well be re-distributed to more stable oxides, such as alumina.

It is known that the component life of both wrought and cast parts is in many cases limited by fatigue failure which often initiates at oxide inclusions.[13] Both agglomerates of small non-metallic particulates as well as flaky Al-rich oxide inclusions may have a significant negative effect on fatigue properties, especially in the high cycle fatigue regime.[2,18,25] Therefore, lowering the amount, but especially the size of non-metallic inclusion defects, is crucial for the spreading of EBM for demanding applications. As shown above, the amount of oxide in the solid samples clearly corresponds to the amount of stable oxides in the powder feedstock. In this respect, addition of virgin powder lowers the overall powder oxygen content which helps to keep down both number and size of oxide inclusions in the solid samples. In addition, as discussed in Reference 24, any possibility to reduce the extent of powder oxidation in the process chamber would be highly beneficial. Finally, a different beam configuration or scan pattern could possibly be used to disrupt oxide accumulation along the scan track

and instead create small dispersed oxides or alternatively, to exaggerate accumulation to locations where they can be easily removed by machining, as suggested in Reference 2.

V. CONCLUSIONS

The following conclusions can be drawn from this study:

- A clear correlation is seen between the amount of oxide inclusions in EBM-processed Alloy 718 and the oxygen level in the feedstock powder, which increases with progressive re-use.
- The main source for oxide defect formation in the EBM-fabricated samples is the Al-rich oxide on the surface of the re-used feedstock powder, which tends to cluster in the liquid metal.
- Owing to transportation and accumulation of oxide during the melting process, the amount of oxide at the top surface and in the contour region of the EBM-fabricated samples is continuously higher than in the hatch region. This has a refining effect on the bulk material which has a lower oxygen level than the powder from which it was fabricated.
- Accumulation of oxide along the electron beam scan direction in samples built from re-used powder increases the amount of LOFDs in the contour region.
- Oxide-containing LOFDs in samples built from re-used powder are not consolidated during hot isostatic pressing.

REFERENCES

1. A.T. Polonsky, M.P. Echlin, W.C. Lenthe, R.R. Dehoff, M.M. Kirka, and T.M. Pollock: *Mater. Charact.*, 2018, vol. 143, pp. 171–81.
2. J.E. Matz and T.W. Eagar: *Metall. Mater. Trans. A*, 2002, vol. 33A, pp. 2559–67.
3. E. Chauvet, P. Kontis, E.A. Jägle, B. Gault, D. Raabe, J.J. Blandin, R. Dendievel, B. Vayre, S. Abed, G. Martin, and C. Tassin: *Acta Mater.*, 2017, vol. 142 (17), pp. 82–94.
4. HE Helmer, C Körner, and RF Singer: *J. Mater. Res.*, 2014, vol. 29 (17), pp. 1987–96.
5. D. Deng: *Additively Manufactured Inconel 718: Microstructures and Mechanical Properties*, Linköping University, Linköping, 2018.
6. W.J. Sames: *Additive Manufacturing of Inconel 718 Using Electron Beam Melting: Processing, Post-processing, & Mechanical Properties*, Texas A&M University, College Station, 2015.
7. X. Wang, X. Gong, and K. Chou: *Proc. Inst. Mech. Eng. Part B*, 2017, vol. 231 (11), pp. 1890–1903.
8. S. Singh: *Varestraint Weldability Testing of Cast Superalloys*, University West, Trollhättan, 2018.
9. N.J. Harrison, I. Todd, and K. Mumtaz: *Acta Mater.*, 2015, vol. 94, pp. 59–68.
10. D. Zhu, X. Zhang, and H. Ding: *Int. J. Mach. Tools Manuf.*, 2013, vol. 64, pp. 60–77.
11. S.L. Cockcroft, T. Degawa, A. Mitchell, D.W. Tripp, and A. Schmalz: "Inclusion precipitation in superalloys", conference proceeding *Superalloys*, 1992, vol. 1992, pp. 577–86.
12. C.S. Yen and T.J. Dolan: *A Critical Review of the Criteria for Notch-Sensitivity in Fatigue of Metals*, University of Illinois, Champaign, 1952, p. 48 bul. 398.
13. C.T. Sims, N.S. Stoloff, and W.C. Hagel: *Superalloys 2*, 2nd ed., Wiley, New York, 1987.
14. M. Yan, P. Yu, in *Sintering Techniques of Materials*, 2015, pp. 77–106.
15. X. Xu, J. Ding, S. Ganguly, C. Diao, and S. Williams: *J. Mater. Process. Technol.*, 2018, vol. 252, pp. 739–50.
16. Y.N. Zhang, X. Cao, P. Wanjara, and M. Medraj: *Acta Mater.*, 2013, vol. 61 (17), pp. 6562–76.
17. L. Thijs, J. Van Humbeeck, K. Kempen, E. Yasa, J. Kruth and M. Rombouts, Innovative Developments in Virtual and Physical Prototyping, 2012, pp. 297–304.
18. H.E. Helmer: Additive Fertigung durch Selektives Elektronenstrahlschmelzen der Nickelbasis Superlegierung IN718: Prozessfenster, Mikrostruktur und mechanische Eigenschaften. Friedrich-Alexander-Universität Erlangen Nürnberg, 2016.
19. L.C. Ardila, F. Garciandia, J.B. González-Díaz, P. Álvarez, A. Echeverria, M.M. Petite, R. Deffley, and J. Ochoa: *Phys. Procedia*, 2014, vol. 56, pp. 99–107.
20. A. Strondl, O. Lyckfeldt, H. Brodin, and U. Ackelid: *Jom*, 2015, vol. 67 (3), pp. 549–54.
21. M. Galati and L. Iuliano: *Addit. Manuf.*, 2018, vol. 19, pp. 1–20.
22. P. Nandwana, W.H. Peter, R.R. Dehoff, L.E. Lowe, M.M. Kirka, F. Medina, and S.S. Babu: *Metall. Mater. Trans. B*, 2016, vol. 47 (1), pp. 754–62.
23. H. Gruber, P. Karimi, E. Hryha, and L. Nyborg: *Powder Metall. Prog.*, 2018, vol. 18 (1), pp. 40–48.
24. H. Gruber, M. Henriksson, E. Hryha, and L. Nyborg: *Metall. Mater. Trans. A*, 2019, vol. 50 (9), pp. 4410–22.
25. D. Krewerth, T. Lippmann, A. Weidner, and H. Biermann: *Int. J. Fatigue*, 2016, vol. 84, pp. 40–52.
26. Haynes, William M., ed. (2016). *CRC Handbook of Chemistry and Physics* (97th ed.). CRC Press, Boca Raton. p. 4.92. ISBN 9781498754293.
27. Maher, *Alloy 718 Data Sheet Quick Facts Alloy 718 Data Sheet Industry Specifications Melting Practices Machinability*. pp. 1–5.
28. P.D. Lee, P.N. Quested, and M. McLean: *Philos. Trans. R. Soc. A*, 1998, vol. 356 (1739), pp. 1027–43.
29. P.N. Quested, D.M. Hayes, and K.C. Mills: *Mater. Sci. Eng. A*, 1993, vol. 173, pp. 369–75.
30. A. Mitchell: *Mater. Sci. Eng. A*, 1999, vol. 263, pp. 217–23.
31. Z.C. Cordero, H.M. Meyer, III, P. Nandwana, and R.R. Dehoff: *Acta Mater.*, 2017, vol. 124, pp. 437–45.
32. A. Mitchell: Progress in understanding clean metal production for IN718, conference proceeding *Superalloys*, 1994, vol. 1994, pp. 109–24.